metals

MDPI

Article

Microstructural Evolution and Creep Behavior of the Weld Interface between 10% Cr Steel and Haynes 282 Filler Metal

Namkyu Kim [1,2], Yongjoon Kang [3], Jinhyeok Bang [3], Sangwoo Song [3], Seong-Moon Seo [4], Chung-Yun Kang [5,*] and Namhyun Kang [2,*]

1 Department of Authorized Nuclear Inspection, Korea Institute of Materials Science (KIMS), Changwon 51508, Korea; nkkim@kims.re.kr
2 Division of Materials Science and Engineering, Pusan National University, Busan 46241, Korea
3 Department of Joining Technology, Korea Institute of Materials Science (KIMS), Changwon 51508, Korea; yjkang@kims.re.kr (Y.K.); bjhyug@kims.re.kr (J.B.); swsong@kims.re.kr (S.S.)
4 Department of High Temperature Materials, Korea Institute of Materials Science (KIMS), Changwon 51508, Korea; castme@kims.re.kr
5 Industrial Liaison Innovation Center, Pusan National University, Busan 46241, Korea
* Correspondence: kangcy@pusan.ac.kr (C.-Y.K.); nhkang@pusan.ac.kr (N.K.)

Abstract: This study investigated the microstructural evolution of the weld interface and creep fracture behavior of 10% Cr martensitic steel welds using Haynes 282 filler metal. The welded joints were subjected to post-weld heat treatment (PWHT) at temperatures of 738 °C for 4, 8, and 15 h. Creep tests were carried out at 600 °C under stress of 200 MPa. The creep rupture life increased with an increase in holding time for PWHT up to 8 h compared to the as-welded condition. However, when the holding time for PWHT was further increased to 15 h, creep properties (i.e., rupture life and creep strain) decreased considerably, and the failure location was found to shift from the ICHAZ to the weld interface. The microstructural investigation revealed that Type I carbides precipitated at the weld interface and recrystallized grains with Cr depletion were formed near Type I carbides in the partially mixed zone during creep exposure. The creep failure at the weld interface began on the surface and propagated inward through the recrystallized grains of the weld-interface region.

Keywords: dissimilar metal welds; weld-interface failure; creep test; post-weld heat treatment; Type I carbide; Cr-depleted region; 10% Cr martensitic steel

check for updates

Citation: Kim, N.; Kang, Y.; Bang, J.; Song, S.; Seo, S.-M.; Kang, C.-Y.; Kang, N. Microstructural Evolution and Creep Behavior of the Weld Interface between 10% Cr Steel and Haynes 282 Filler Metal. *Metals* **2021**, *11*, 764. https://doi.org/10.3390/met11050764

Academic Editor: Elisabetta Gariboldi

Received: 20 April 2021
Accepted: 4 May 2021
Published: 6 May 2021

Publisher's Note: MDPI stays neutral with regard to jurisdictional claims in published maps and institutional affiliations.

Copyright: © 2021 by the authors. Licensee MDPI, Basel, Switzerland. This article is an open access article distributed under the terms and conditions of the Creative Commons Attribution (CC BY) license (https://creativecommons.org/licenses/by/4.0/).

1. Introduction

In the steam-generating systems of fossil fuel power plants, high-chromium (9–12% Cr), martensitic, heat-resistant steels have been widely used as structural materials at elevated temperatures [1,2]. Currently, enhancing the operating efficiency of power plants by increasing the service temperature and pressure is necessary because of environmental and economic considerations. Power plants operating at ultra-supercritical (USC) or advanced USC (A-USC) conditions require heat-resistant materials with enhanced creep resistance at temperatures above 600 °C [3]. To achieve the required mechanical properties at the service temperature and reduce the cost, Ni-based superalloys are employed for high-temperature applications above 650 °C, whereas advanced high-chromium (9–12% Cr) martensitic steels are used at temperatures lower than 650 °C [4]. Using different types of materials within the systems requires a dissimilar metal weld (DMW) joint. Ni-based filler metal is preferred for joining the DMWs between Ni-based alloys and 9–12% Cr martensitic steels because of its low carbon solubility, high ductility, and excellent solidification cracking resistance [5].

For successful long-term application in a high-temperature environment, it is necessary to investigate the microstructural change across the welded joint and its effect on creep properties. The creep rupture of DMWs between 9–12% Cr steels and Ni-based alloys

commonly occurs on the steel side because of its relatively lower creep strength [6–8]. It is reported that premature creep rupture of 9–12% Cr martensitic steel welded joints typically occurs in the fine-grained heat-affected zone (FGHAZ) or intercritical HAZ (ICHAZ), known as Type IV failure [9].

Type IV cracking is related to softening of the HAZ, coarsening of precipitates, formation of Laves phase, and lack of sufficient precipitates pinning at the grain boundaries [8–10]. The welded joints of 9–12% Cr martensitic steels are generally subjected to post-weld heat treatment (PWHT) to remove the heterogeneity in microstructure and to recover the mechanical properties of the welds. Our recent study demonstrates that Type IV failure resistance improves with an increase in holding time for PWHT up to 8 h at 738 °C because of the combined effect of microstructural homogenization and suppression of the Laves phase formation in the ICHAZ [11]. A longer holding time for PWHT at 738 °C was assumed to be required for optimal creep properties. However, when the holding time for PWHT was increased to 15 h, creep properties decreased considerably, and the failure location was found to shift from the ICHAZ to the weld interface. Consequently, there is a need for the proper selection of PWHT condition to obtain the optimum combination of microstructure and mechanical properties in accordance with the final requirement of intended application.

Several authors have reported the possible causes of interface failure of DMWs: (1) a large difference in the coefficient of thermal expansion (CTE) between the ferritic and austenitic alloys [12,13], (2) creep voids nucleation and growth around Type I carbides [13–15], (3) oxide notch formation at the interface [8,13,16,17], and (4) a sharp change in microstructure and mechanical properties across the fusion line [13,18,19]. However, the mechanism of a weld-interface premature failure has not been fully investigated, specifically in DMWs.

This study focuses on the microstructure evolution of the weld-interface region for as-welded, PWHTed, and creep tested conditions. Specifically, the mechanism of Type I carbides formation and their effect on the interface failure in the DMWs of 10% Cr steel using Haynes 282 filler metal were explored.

2. Experimental Procedures

2.1. Materials, Welding Procedure, and PWHT Conditions

The material used in this study was a 10% Cr martensitic steel plate with a thickness of 10 mm. It was normalized at 1100 °C for 1 h and tempered at 700 °C for 30 h. We reported previously that the 10% Cr steel base metal (BM) consisted of a typical tempered martensite structure with coarse Cr-rich $M_{23}C_6$ and fine V-rich MC precipitates [20]. The A_{C1} and A_{C3} transformation temperatures measured by a differential scanning calorimeter (DSC, NETZSCH 404C, Selb, Germany) were 852 and 895 °C, respectively. Haynes 282 was used as a welding wire. Chemical compositions of the as-received 10% Cr steel and Haynes 282 filler are listed in Table 1.

Table 1. Chemical composition of the 10% Cr steel BM and Haynes 282 filler metal.

	Chemical Compositions (wt%)										
	C	**Cr**	**Co**	**Mo**	**W**	**V**	**Nb**	**Ti**	**Al**	**Fe**	**Ni**
10% Cr Steel	0.08	9.8	2.7	0.7	1.6	0.2	0.06	-	-	Bal.	0.05
Haynes 282	0.06	19.44	10.28	8.5	-	-	-	2.22	1.47	0.32	Bal.

Welding was performed using the automatic gas tungsten arc welding (GTAW) process with pure Ar gas as the shielding gas. A single V-groove of 60° (7 mm in depth) was prepared for weld deposition. A detailed weld preparation and welding process were described in the previous study [11]. The voltage and current used in the welding process were 10–14 V and 236–240 A, respectively. A summary of welding conditions used is given in Table 2.

Table 2. Welding conditions applied to produce DMWs.

Welding Current (A)	236–240
Voltage (V)	10–12 (1st pass) 11–14 (2nd pass)
Welding speed (mm/s)	2.0
Shielding gas	Pure Ar
Preheat temp.	N/A
Interpass temp. (°C)	48
Filler metal dia. (mm)	2.4

Section I in the ASME Boiler and Pressure Vessel Code requires the PWHT of 9–12% Cr steels to be carried out in a temperature range of 675–785 °C. After welding, the PWHT was carried out at 738 °C for a holding time of 4, 8, and 15 h. The temperature of 738 °C is in the normally recommended PWHT temperature range for 9–12% Cr steels and lower than the A_{C1} temperature of the BM.

2.2. Creep Testing

Creep tests were performed at 600 °C with an applied stress of 200 MPa using an ATS (series 2300) machine. Cylindrical specimens with a gauge diameter of 4 mm and a gauge length of 25 mm were employed for creep tests. The welded joint was in the center of the specimen and within the gauge length, as described in our recent work [11]. To investigate the weld-interface cracking mechanism, creep interruption testing was conducted at 630 °C under the stress of 150 MPa for the welded joint with a PWHT temperature of 738 °C for 15 h.

2.3. Microstructural Characterisation

Metallographic examinations of the welded joints were carried out under the as-welded, PWHTed, and creep tested conditions using a light optical microscope (LOM, Olympus_BX53M, Tokyo, Japan), scanning electron microscope (SEM, JSM_7001F, Akishima, Japan), and field emission scanning transmission electron microscope (FE-STEM, Thermo Fisher Scientific Talos F200X, Waltham, MA, USA). For the microstructure characterization by LOM and SEM, the specimens were polished and etched in Vilella's reagent (1 g picric acid + 5 mL HCl + 100 mL ethanol). Backscattered electron (BSE) images of SEM were used to distinguish the W and Mo-rich Laves phase (bright contrast) from $M_{23}C_6$ particles (dark contrast) [21]. A TEM microanalysis of the weld-interface region was performed on the specimens prepared by the focused ion beam (FIB, Thermo Fisher Scientific Scios2, Waltham, MA, USA) technique. Selected area electron diffraction (SAED) was used to determine the crystal structure of the phase.

The chemical compositions and element distribution were analyzed by energy dispersive spectroscopy (EDS) and electron probe microanalysis (EPMA), respectively. The location of the FCC/BCC interphase boundary was identified via an electron backscatter diffraction (EBSD) phase map, and a kernel average misorientation (KAM) analysis was used to evaluate the strain accumulation in the weld-interface region. Variation in austenite transformation temperature (A_3) across the weld-interface region was determined by Thermo-Calc software (Stockholm, Sweden) using the TCFE9 database.

3. Results and Discussion

3.1. Effect of PWHT Holding Time at 738 °C on Creep Rupture Behaviour

Creep curves of the 10% Cr steel DMWs under various PWHT conditions are shown in Figure 1. The as-welded specimen ruptured at 2763 h (~40% below base metal). The specimens with a PWHT temperature of 738 °C for 4 and 8 h were ruptured at 3242 and 5043 h, respectively. However, for the specimen with a PWHT temperature of 738 °C for 15 h, the creep properties (rupture life and creep strain) decreased considerably. The variations in the creep rupture life and strain under the various PWHT holding time at

738 °C are shown in Figure 2. All the welded joints exhibited lower creep properties compared to the 10% Cr steel BM.

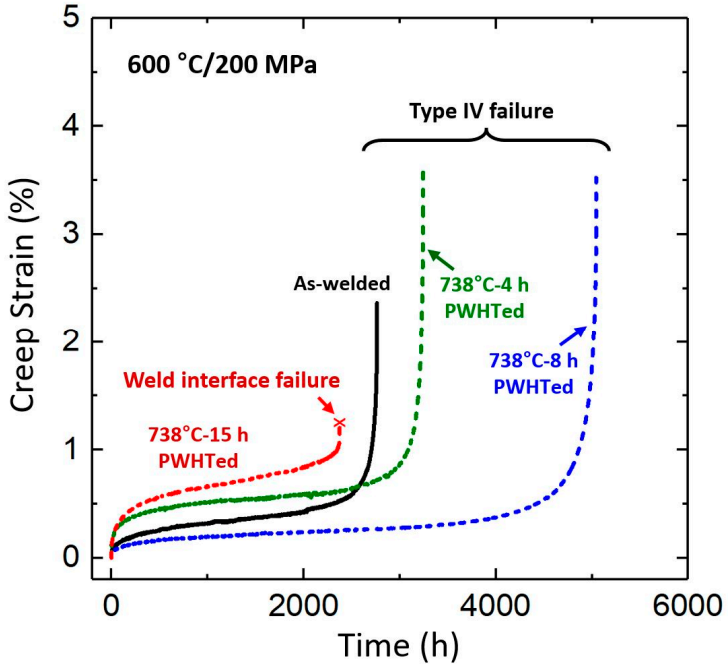


Figure 1. Comparison of the creep curves at 600 °C/200 MPa under various PWHT conditions.

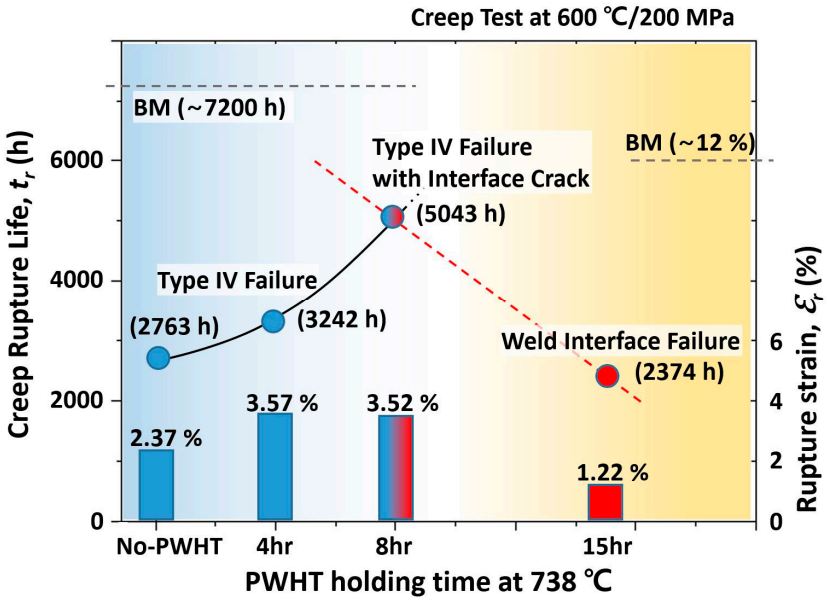


Figure 2. Comparison of the creep properties at 600 °C/200 MPa as a function of PWHT holding time at 738 °C.

Figure 3 shows the failure location of ruptured specimens subjected to creep deformation. The as-welded (no PWHT) specimen that was ruptured at 2763 h was fractured in the ICHAZ (close to the FGHAZ), commonly known as Type IV failure [9]. The creep rupture life increased with an increase in PWHT holding time up to 8 h compared to the as-welded condition. The specimens with a PWHT temperature of 738 °C for 4 and 8 h were also fractured in the ICHAZ (Figure 3a,b).

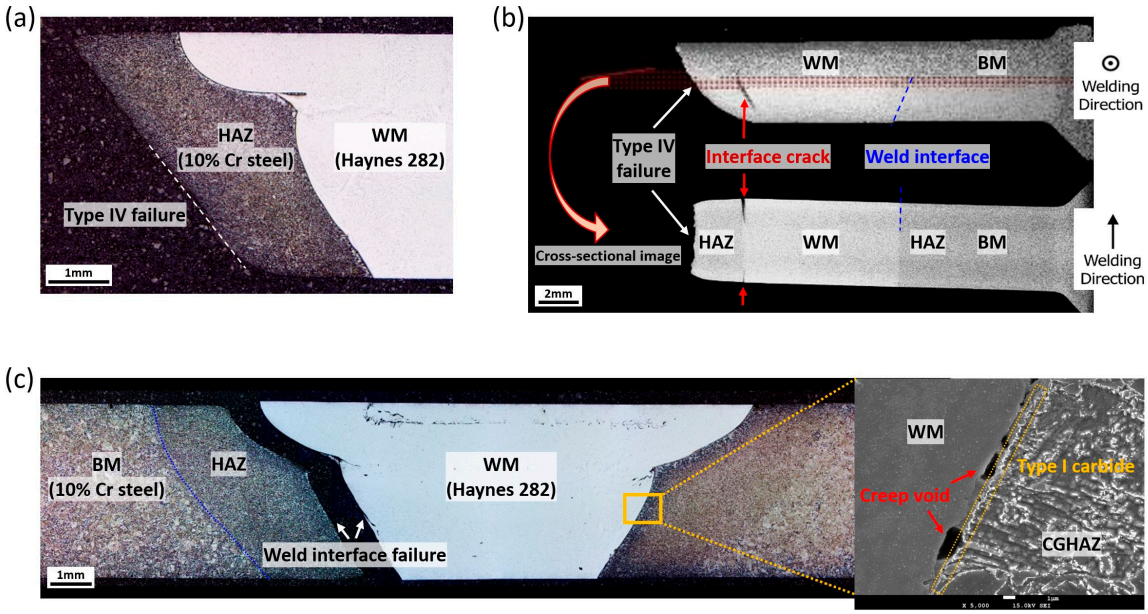


Figure 3. Cross-sectional images after creep test at 738 °C with different PWHT holding times: (**a**) 4 h; (**b**) 8 h (X-ray micro-CT image); and (**c**) 15 h.

For the specimen with a PWHT temperature of 738 °C for 15 h, the creep properties (rupture life and creep strain) decreased considerably, and the failure location was found to shift from the ICHAZ to the weld interface (Figure 3c). Moreover, on the opposite side of the fractured surface, Type I carbides and creep voids were observed along the weld interface after the creep test. Remarkably, a small notch was observed at the weld interface in the 738 °C-8 h PWHTed creep specimen, even though the Type IV failure occurred in the ICHAZ with the maximum creep life (t_r: 5043 h), and the interface crack propagated along the weld interface from the specimen surface (Figure 3b). This implies that the preferential accumulation of creep deformation occurred at both the ICHAZ and the weld interface. Our previous study reported that Type IV failure resistance improved with increasing PWHT holding time at 738 °C, owing to the combined effect of a homogenized microstructure and suppression of the Laves phase formation in the ICHAZ [11]. Therefore, sufficient PWHT at 738 °C could concentrate more stress/strain at the weld interface rather than in the ICHAZ during the creep test.

3.2. Microstructure Evolution and Type I Carbide Formation at the Weld Interface

The microstructure and EPMA analysis results across the weld-interface region under the as-welded condition are shown in Figure 4. In the coarse-grained HAZ (CGHAZ) near the fusion boundary, most of the precipitates dissolved in the matrix because of high peak temperature for welding, and the structure transformed first to austenite and then to martensite [22,23]. Within the fusion zone near the fusion line, a partially mixed zone (PMZ, ~15 μm in width) formed. In this zone, the composition changed gradually from that of the fusion zone to that of the BM [13,24,25]. In the PMZ (Figure 4b), Ni and Cr contents increased, and Fe content decreased from the 10% Cr steel BM toward the Haynes 282 weld metal (WM). The weld interface between WM and CGHAZ is indistinct because an increase in Cr and Ni contents at the weld interface makes this region resistant to etching by Villela's reagent (Figure 4a).

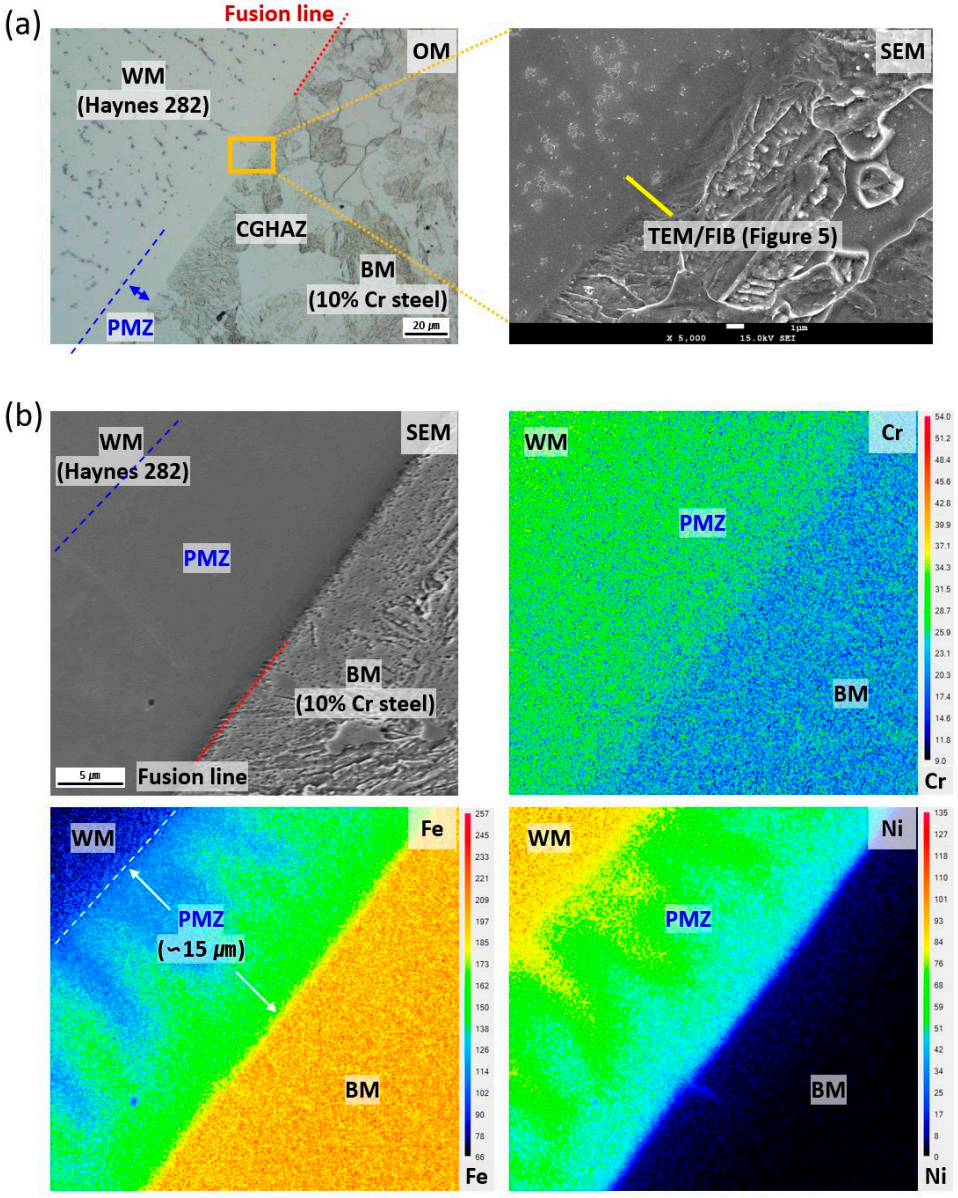


Figure 4. Microstructure and compositional distribution of the weld-interface region under the as-welded condition: (**a**) LOM and SEM images and (**b**) EPMA analysis.

To investigate the detailed-microstructural characteristics of the weld-interface region, an FIB specimen for the TEM analysis was extracted from the fusion boundary marked by a yellow line in Figure 4a. Figure 5a shows a bright-field TEM image with an EDS line analysis. The interface band (~0.5 μm in width) was observed in the PMZ adjacent to the fusion boundary; however, there were no abrupt chemical composition changes across the interface band. The SAED of the WM corresponded to the FCC structure because of the Haynes 282 filler metal (Figure 5b). However, the interface band was confirmed as the BCC structure by a SAED analysis (Figure 5c). The chemical composition in the interface-band region is similar to the HAZ because insignificant mixing occurred with the filler metal, but it had a slightly high Ni content. The Ni element, a strong stabilizer of FCC, tends to decrease martensite start (Ms) temperature [13,19]. During welding, the 10% Cr steel HAZ adjacent to the WM was austenitized (FCC in structure) where temperature exceeded the austenite transformation temperature (A_3). Upon cooling, a martensitic transformation (BCC in structure) occurred in the HAZ (Figure 5d). As the cooling progressed, it was expected that the interface-band region subsequently transforms

into martensite. Martensite transformation did no longer form in the fusion zone where Ms temperature dropped below room temperature. The interface band consisted of FCC/BCC boundary and fusion boundary, respectively, for the WM and BM sides.

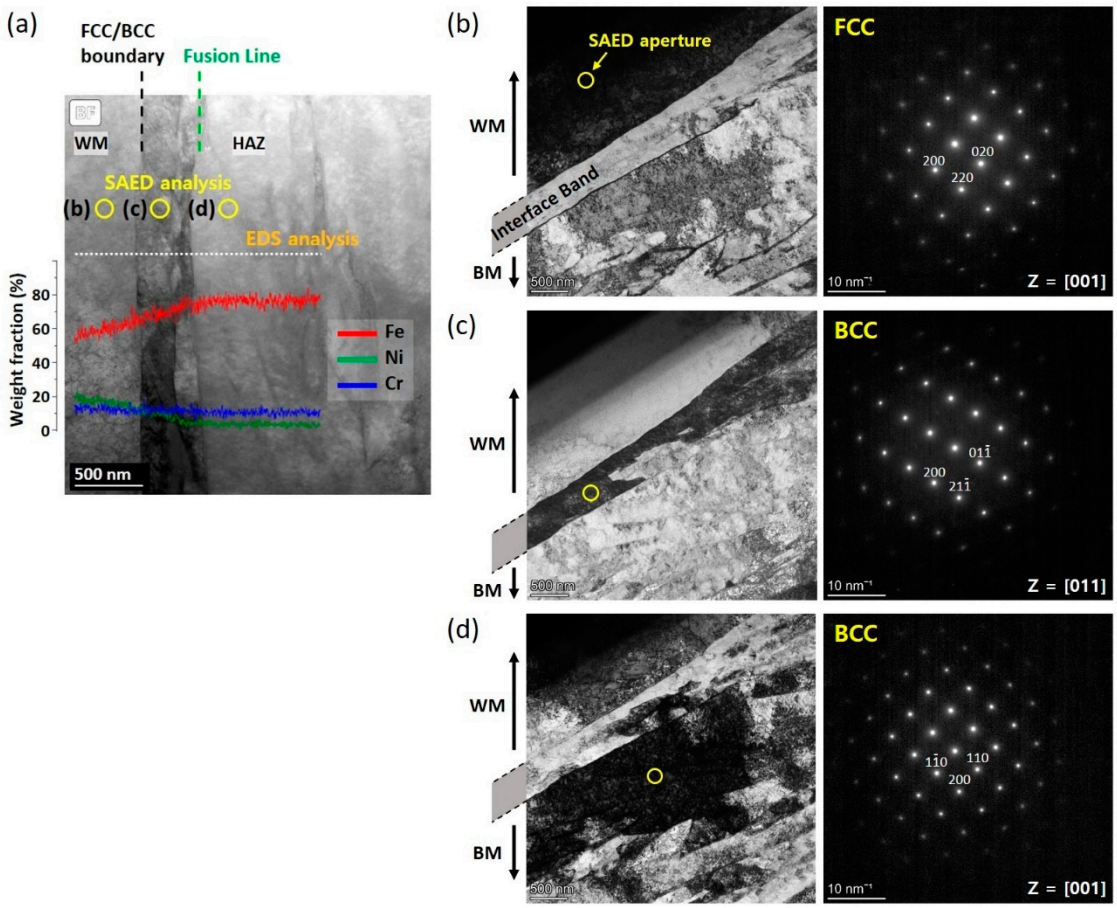


Figure 5. Interface-band region under the as-welded condition: (**a**) TEM microstructure, (**b**–**d**) SAED analysis of WM, interface band, and HAZ, respectively.

The SEM microstructure and EDS analysis results of the weld-interface region after PWHT at 738 °C for 15 h are shown in Figure 6a. The PWHT changed the martensite to the tempered martensite, consisting of the precipitates in the HAZ. Large Cr-rich $M_{23}C_6$ carbides were distributed along the grain, packet, and block boundaries. Furthermore, small Cr-rich $M_{23}C_6$ carbides were observed near the weld interface in a row, which is known as Type I carbides [13,26]. Importantly, precipitates were not observed between the FCC/BCC boundary and the row of Type I carbides. Figure 6b shows TEM/EDS analysis results of the FIB specimen extracted from the fusion boundary marked by a yellow line in Figure 6a. The bright-field (BF) TEM image and EDS elemental mapping results correspond well with the Cr-rich carbides distribution. The chemical composition in the interface-band region along the white dotted line (Figure 6b) showed an abrupt increase in Cr near the weld interface. Type I and small Cr-rich carbides were produced ~0.3 μm away from the FCC/BCC boundary within the interface band.

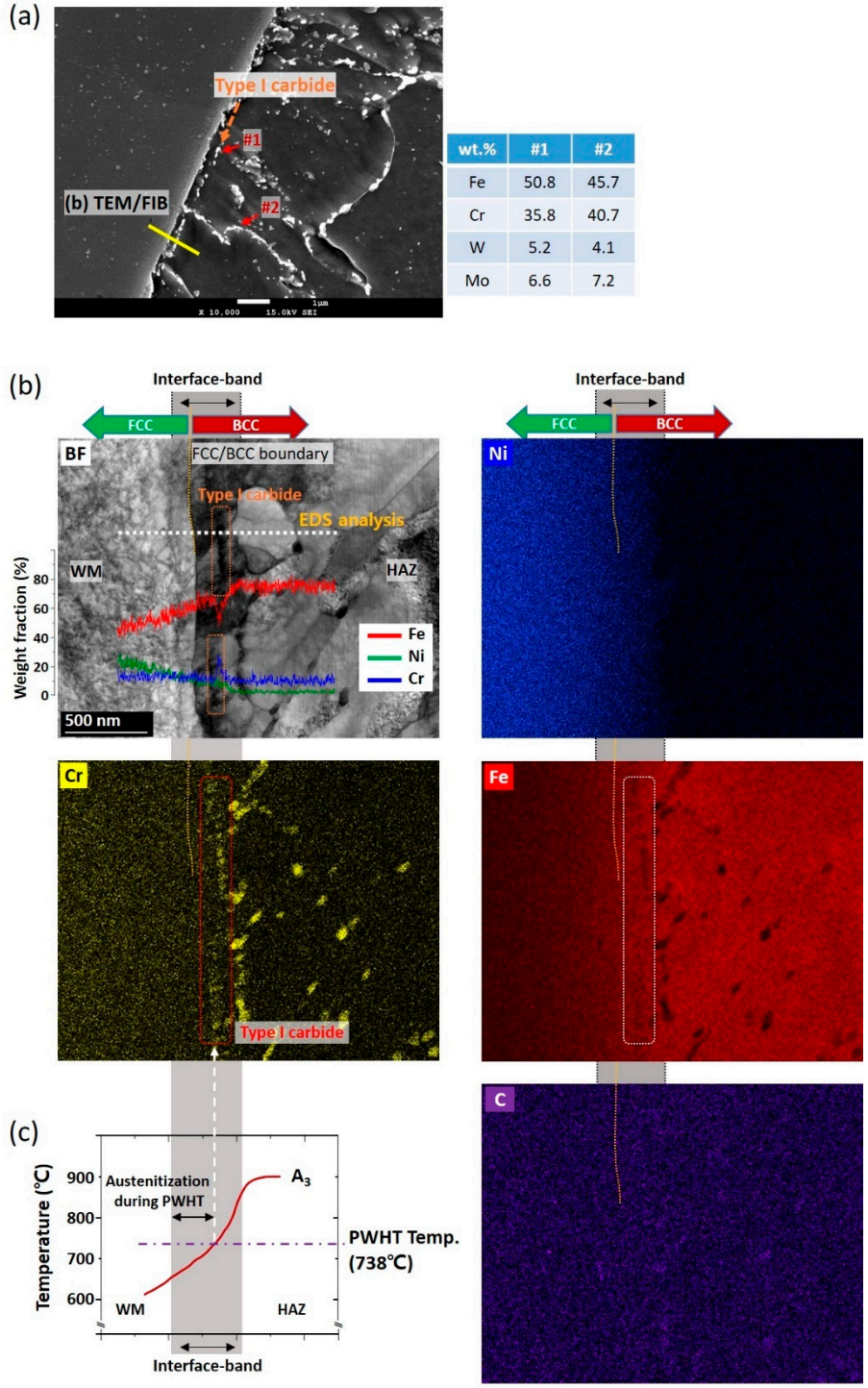


Figure 6. Microstructure and compositional distribution of the weld-interface region after PWHT at 738 °C for 15 h: (**a**) SEM microstructure (including EDS analysis of the precipitates marked with red arrows); (**b**) TEM bright-field image and EDS elemental maps for Cr, Ni, Fe, and C; and (**c**) A_3 temperature variation calculated by Thermo-Calc software.

Figure 7 shows the nano-indentation and EBSD (phase map, unique grain color map and KAM) analysis of the weld-interface region after PWHT at 738 °C for 15 h. Because the depth of the nano-indentation tip was extremely small (~200 nm), the nano-indentation test was performed on the as-polished specimens (i.e., before etching). The HAZ hardness decreased considerably after PWHT because of the evolution of precipitates as a result of a tempering reaction and the formation of tempered martensite [27]. The phase map

indicated a BCC and FCC, respectively, in HAZ and WM, and the KAM showed that considerable strain accumulated in HAZ, therefore confirming that the HAZ was occupied with tempered martensite. Importantly, however, fine grains (~0.5 μm width) with a locally high hardness value were observed inside the weld interface.

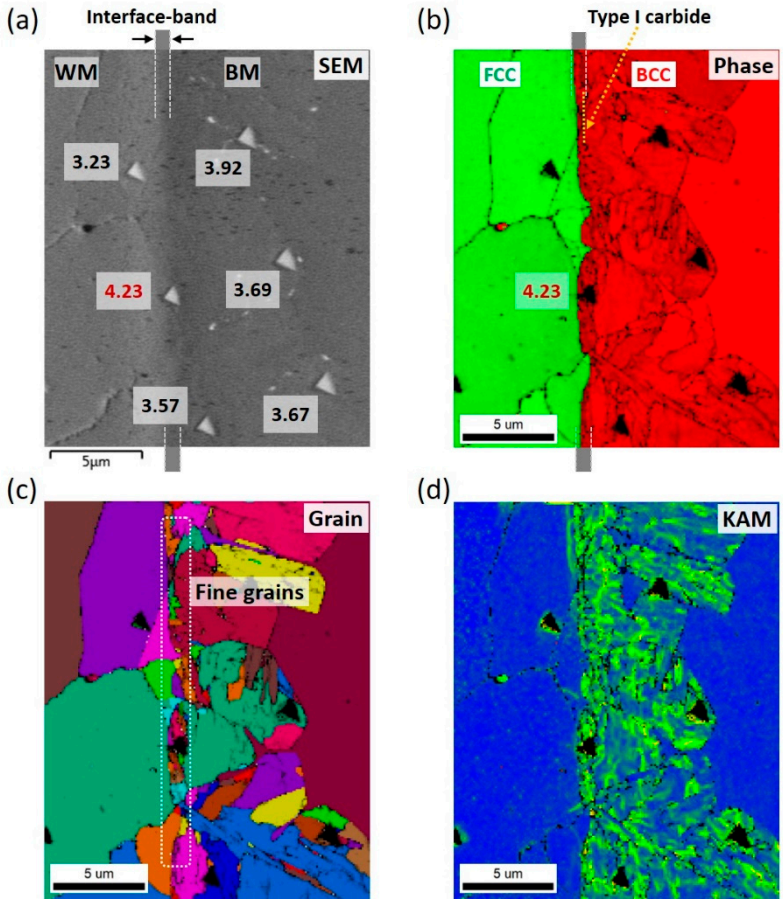


Figure 7. Microstructure and nano-indentation of the weld-interface region after PWHT at 738 °C for 15 h: (**a**) Forward scatter detector (FSD) image after the nano-indentation test (hardness values are presented in the figure) and (**b**–**d**) EBSD analysis of phase map, unique grain color map, and KAM, respectively.

Detailed composition analysis was conducted to identify the mechanism of the fine grain and Type I carbide formation. A comparison of Figures 5a and 6a reveals that the chemical composition in the interface-band region after PWHT is similar to that in the as-welded region except for the $M_{23}C_6$ carbide. Using the chemical composition measured by TEM/EDS across the weld-interface band under as-welded condition (Figure 5a), the variation in austenite transformation temperature (A_3) was thermodynamically calculated by Thermo-Calc software (Figure 6c). The A_3 temperature normally decreases with increasing Ni content [18,19]. It is assumed that a portion of the interface band with relatively high Ni content was austenitized during the PWHT at 738 °C because the A_3 temperature was lower than the PWHT temperature. Therefore, fine-grained austenite could form in the interface band near the WM, which subsequently transforms into fine martensite on cooling from the PWHT temperature. Shin et al. [18] and Falat et al. [3] also reported the formation of martensite at the fusion boundary after PWHT. The newly formed fine martensite was considered for the higher hardness of the weld interface than the neighboring regions (Figure 7a). During the PWHT, large numbers of precipitates were formed at the grain/packet/block boundaries of the CGHAZ (Figure 6a). However, a precipitate-free matrix was observed in the fine grain newly formed from the interface band because that

region should be austenite during PWHT, which has a high solubility for carbon [13,14]. Thus, Type I carbides (a series of small $M_{23}C_6$ carbides) formed preferentially along BCC (fresh martensite of the interface band near the WM)/BCC (tempered martensite of the interface band near the BM) boundary during cooling from the PWHT temperature.

The evolution of the weld-interface band was observed after welding, and it is associated with Ms temperature changes owing to the chemical-composition gradient in the PMZ. During PWHT, the austenitized-fine grain led to the formation of a row of carbides (Type I carbides) in the interface-band region. Figure 8 schematically illustrates the development of the weld-interface band and Type I carbide. During welding, PMZ was formed near the BM (Figure 8a). After welding, the interface band was formed in the PMZ, and it was solidified as austenite and then transformed to martensite (Figure 8b). During PWHT, $M_{23}C_6$ carbides were precipitated along the grain/packet/block boundary in the HAZ, and small Type I carbides were distributed along FCC (austenite)/BCC (martensite) grain boundary (Figure 8c). After PWHT, numerous small Type I carbides were formed along BCC (fresh martensite)/BCC (tempered martensite) boundary on cooling from the PWHT temperature (Figure 8d).

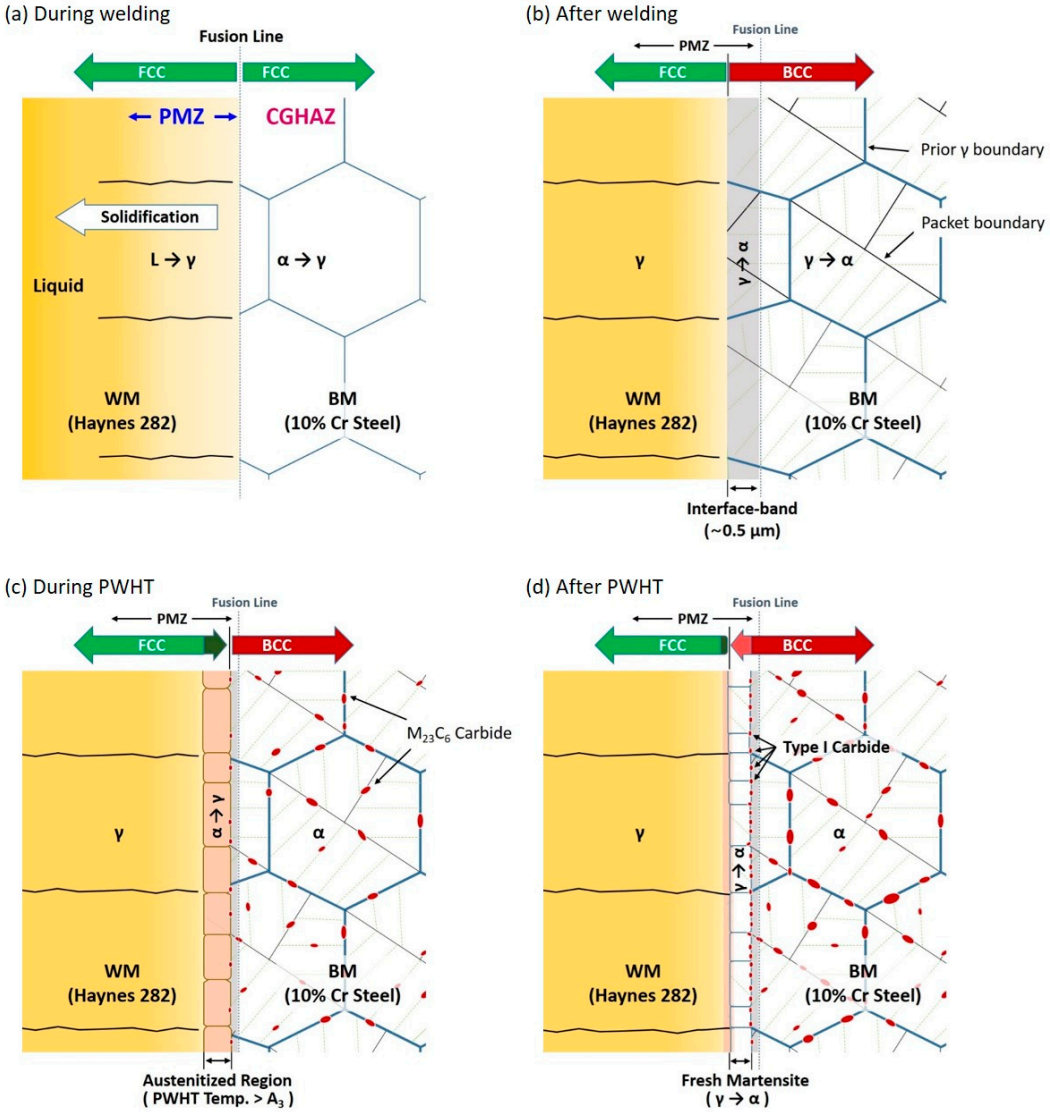


Figure 8. A schematic illustration of possible microstructure evolution and Type I carbide precipitation at the weld interface during welding and PWHT: (**a**) during welding, (**b**) after welding, (**c**) during PWHT, and (**d**) after PWHT.

3.3. Weld Interface Creep Failure Mechanism

Figure 9a shows the SEM microstructure of the weld-interface region (non-fractured side) of the 738 °C-15 h PWHTed specimen after the creep test at 600 °C with applied stress of 200 MPa. The corresponding BSE image is shown to distinguish the W and Mo-rich Laves phase (bright contrast) from the Cr-rich $M_{23}C_6$ particles (dark contrast). Some Laves phase ($(Fe, Cr)_2(W, Mo)$) particles were distributed with the $M_{23}C_6$ carbides. The precipitation of the Laves phase is normally considered to reduce the creep strength because the nucleation and growth of the Laves phase are promoted by the diffusion of W or Mo from the matrix to the Laves phase, which results in the loss of solid solution strengthening [28]. The Type I carbides after creep rupture were much coarser than the $M_{23}C_6$ carbides in the CGHAZ before the creep test. This implies that additional precipitation of the $M_{23}C_6$ carbides in the newly formed martensite occurred mostly near the Type I carbides during creep exposure at 600 °C.

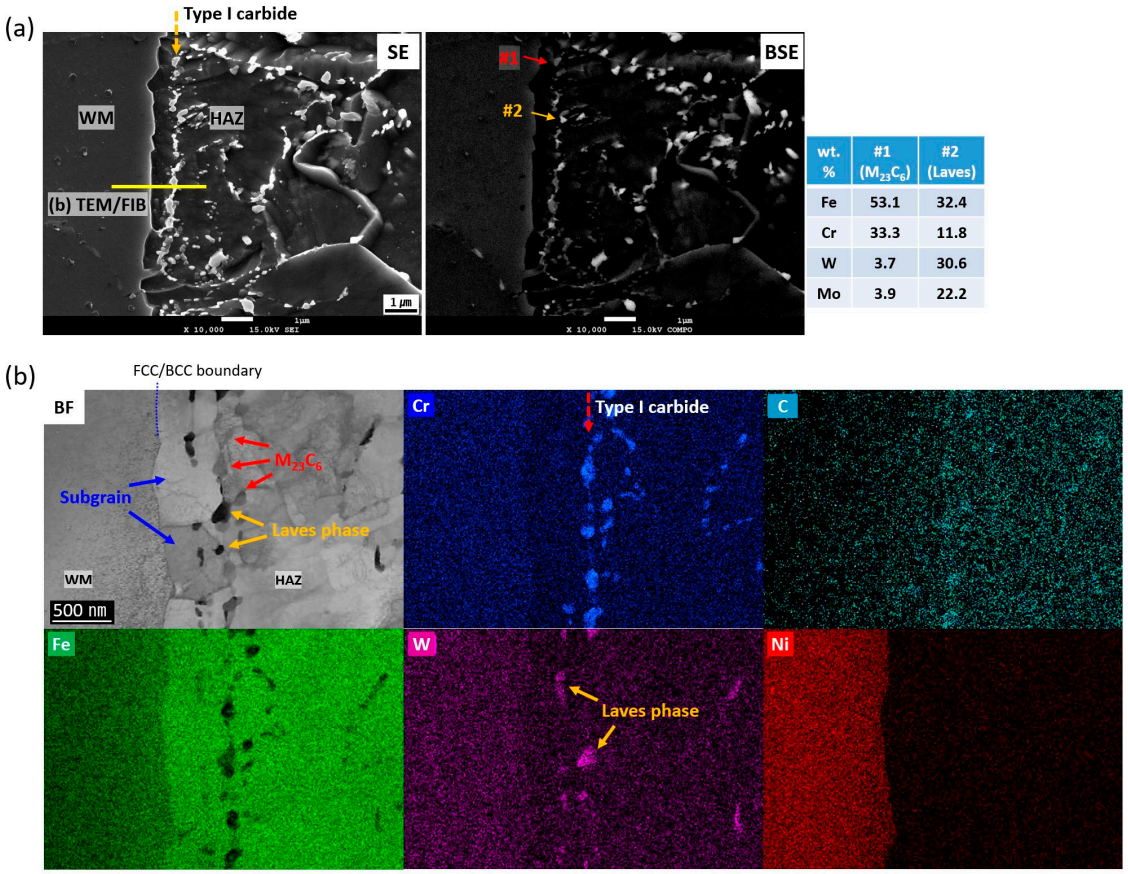


Figure 9. Microstructure of the weld-interface region of the 738 °C-15 h PWHTed specimen after the creep test: (**a**) SEM and BSE image (including EDS analysis of the precipitates marked with arrows) and (**b**) TEM bright-field image and EDS elemental maps for Cr, C, Fe, W, and Ni.

Figure 9b shows TEM/EDS analysis of the FIB specimen, which was extracted from the fusion boundary after the creep test as indicated with a yellow line in Figure 9a. A bright-field TEM image revealed that polygonal subgrains were only formed within the interface band, implying that significant local recovery occurred in this region during the creep test. This is attributed to the refinement of the prior austenite grain (PAG) size before creep. Morito et al. [29] and Takaki et al. [30] showed that the martensite structure has only one packet/block whose PAG size was less than 2 and 1 μm, respectively. The packet/block number is considerably reduced when the PAG size is below 10 μm [31,32]. Owing to the limited packet/block boundaries, $M_{23}C_6$ carbides were preferentially nucleated and grown on those PAG boundaries along the Type I carbides during creep exposure. The

TEM/EDS elemental mapping confirmed that Type I carbides and Laves phase particles were distributed along the recrystallized grain boundary (Figure 9b). Precipitates of the packet and block boundaries in the martensitic steel play a significant role in maintaining its high creep strength by stabilizing the subgrain structure against coarsening and recrystallisation [33]. Thus, the fine-martensite grain without packet and block boundaries underwent extensive recovery and subgrain growth by reducing the pinning effect.

Figure 10 shows the segregation of Cr, W, and Mo elements to the grain/packet/block boundaries measured by EPMA. The higher concentration of Cr along the weld interface is associated with the Type I carbide, and the Cr-depleted region formed in the interface-band region was observed near the row of Type I carbides. At the weld interface, additional precipitation of the Cr-rich $M_{23}C_6$ carbides expense Cr solutes from the matrix adjacent to the carbides during creep exposure occurred, which resulted in the formation of the Cr-depleted region near the Type I carbides. Remarkably, the creep voids were observed along the Cr-depleted region of the weld-interface region. Furthermore, the high W and Mo concentrations contributed to the formation of Laves phase precipitates near the Type I carbides (Figure 9b).

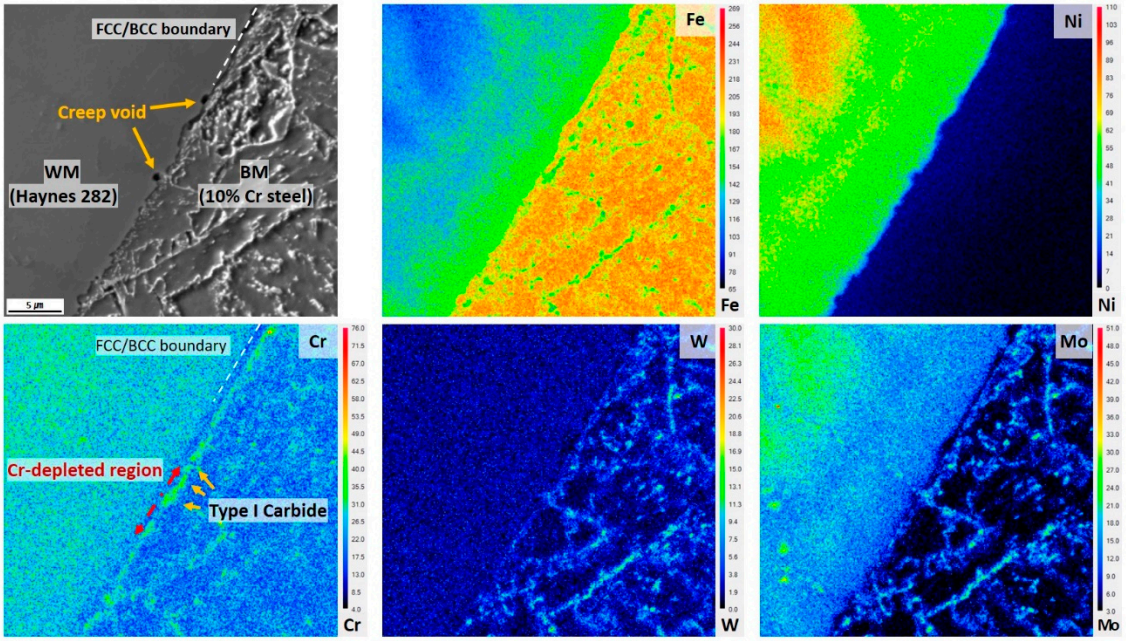


Figure 10. SEM image and EPMA analysis of the weld-interface region after the creep test.

To investigate the microstructure evolution and failure mechanism of weld interface during creep exposure, a creep interruption test was conducted. Figure 11 shows the SEM and EBSD (phase map, unique grain color map, and KAM) analysis results of the weld interface near the crack tip after the creep interruption test for 1600 h (creep strain ~ 1%). Numerous creep voids were observed between the FCC/BCC boundary and the row of Type I carbides along the weld interface (marked with yellow arrows in Figure 11a). Figure 11b shows the weld-interface region undergoing a considerable decrease in strain accumulation during the creep test. In comparison with Figure 7b–d (before the creep test), the microstructures of the weld-interface region were completely recrystallized after the creep test. Creep-void nucleation is typically associated with the stress/strain concentration. Laha et al. [7,19] and Krojer et al. [3] showed that the preferential concentrations of the creep deformation were observed in the ICHAZ and the weld-interface region. By applying prolonged PWHT at 738 °C, a homogenized microstructure of the 10% Cr steel HAZ was obtained [11]. Thus, the stress concentration was higher at the weld interface than in the ICHAZ. Moreover, the strength of the weld-interface region decreased by the loss of the solid solution strengthening effect of Cr, W, and Mo owing to the formation of the Cr-rich

Type I carbides and Laves phase during creep exposure. Therefore, the soft recrystallized grains of the interface region were preferentially deformed under the applied creep stress in the study. The discontinuities such as Type I carbides, Laves phase particles, and FCC/BCC interphase boundary provided preferred nucleation sites for creep voids.

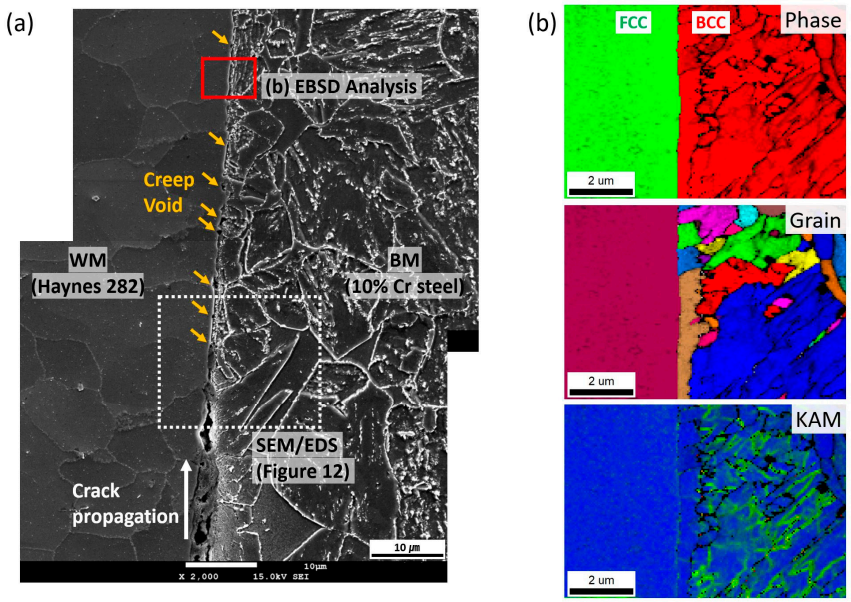


Figure 11. Creep-void formation in the weld-interface region near the crack tip after the creep interruption test: (**a**) SEM image and (**b**) EBSD analysis (phase map, unique grain color map, and KAM).

For all the creep specimens with weld interface cracking, interface cracking always initiated from the surface and propagated inward through the subgrains between the FCC/BCC boundary and the row of Type I carbides (Figures 3b and 11a). Figure 12 shows the SEM/EDS elemental distribution of the crack-propagation region at the weld interface. Oxidation along the interface crack was observed. The oxide notch is known to be produced at the interface and it leads to interfacial failure by the growth of the oxide [8,16,17]. Because of the relatively poor oxidation resistance of the Cr-depleted region and the difference in creep strength between austenitic WM and ferritic BM, uncoordinated deformation should induce an oxide-notch initiation [8,34]. In the presence of geometric discontinuities such as notches, localized creep takes place in a small region near the notch root [35,36]. Once a crack was initiated ahead of the oxide notch, crack propagation occurred along the soft recrystallized grains of the weld-interface region under the external creep stress (Figure 11a), providing fresh surface to be exposed to the air to promote the oxidation. Moreover, crack propagation through this interface region became dominant by the creep voids formed ahead of the crack.

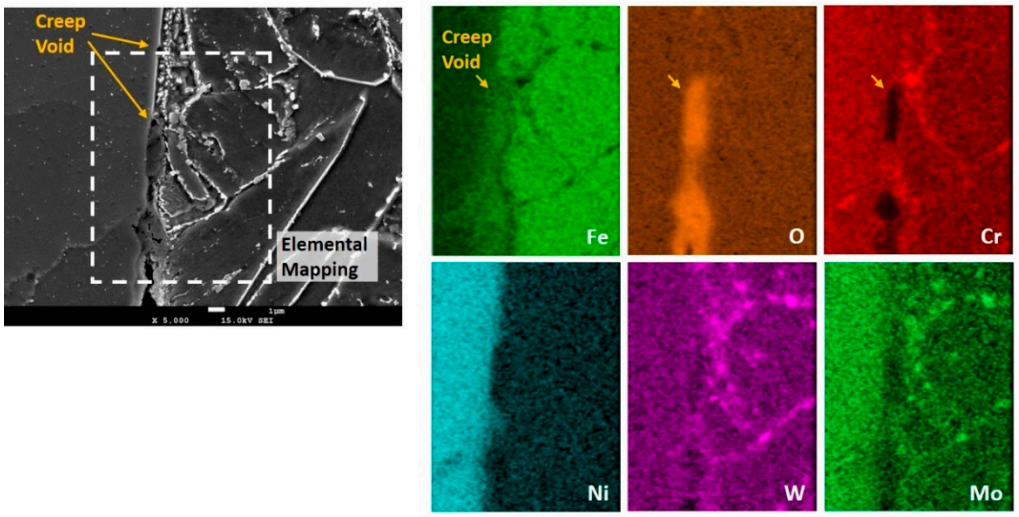


Figure 12. Microstructure and elemental maps (for Fe, O, Cr, Ni, W, and Mo) of the crack propagation region at the weld interface after the creep interruption test.

4. Conclusions

In this study, the microstructural evolution of the weld interface was associated with the creep fracture behavior of 10% Cr steel welds using Haynes 282 Ni-based filler metal. The creep tests were carried out at 600 °C under a stress of 200 MPa, and it was found that excessive PWHTs accelerated the premature failure of the weld interface. The main conclusions are as follows:

The creep life of the PWHTed joints at 738 °C increased with an increase in the PWHT holding time up to 8 h compared to the as-welded condition. However, when the holding time for PWHT was increased further to 15 h, creep properties decreased considerably, and the failure location was found to shift from the ICHAZ (Type IV failure) to the weld interface.

The evolution of Type I carbides was observed after PWHT, and it is associated with the austenitized fine grain in the weld-interface band during PWHT, owing to the chemical-composition gradient in the PMZ.

During creep exposure, the weld-interface region produced a soft subgrain structure and poor oxidation resistance owing to the extensive recovery and additional Cr-rich Type I carbides formation, respectively.

Weld-interface failure was initiated by an oxide notch on the surface of the Cr-depleted region in the weld-interface region and then propagated along the soft recrystallized grains of the weld interface by stress/strain concentration under the creep stress.

Author Contributions: Conceptualization, N.K. (Namkyu Kim), C.-Y.K., and N.K. (Namhyun Kang); methodology, N.K. (Namhyun Kang); software, N.K. (Namkyu Kim) and Y.K.; validation, S.S., C.-Y.K., and N.K. (Namhyun Kang); formal analysis, J.B.; investigation, N.K. (Namkyu Kim), Y.K., and S.-M.S.; resources, N.K. (Namkyu Kim); data curation, N.K. (Namkyu Kim), J.B., and S.S.; writing—original draft preparation, N.K. (Namkyu Kim), Y.K., and S.-M.S.; writing—review and editing, S.S., C.-Y.K., and N.K. (Namhyun Kang); visualization, J.B.; supervision, C.-Y.K. and N.K. (Namhyun Kang). All authors have read and agreed to the published version of the manuscript.

Funding: This research received no external funding.

Institutional Review Board Statement: Not applicable.

Informed Consent Statement: Not applicable.

Data Availability Statement: Not applicable.

Acknowledgments: This work was supported by the National Research Foundation of Korea (NRF) grant funded by the Korea government (MSIT) [NRF-2019M2D2A205091812], and by the Korea

Institute of Energy Technology Evaluation and Planning (KETEP) and the Ministry of Trade, Industry, and Energy (MOTIE) of the Republic of Korea [20206500000010].

Conflicts of Interest: The authors declare no conflict of interest.

References

1. Abe, F. Creep Behavior, Deformation Mechanisms, and Creep Life of Mod.9Cr-1Mo Steel. *Met. Meter. Trans. A* **2015**, *46*, 5610–5625. [CrossRef]
2. Sakthivel, T.; Laha, K.; Vasudevan, M.; Koteswara Rao, M.; Panneer Selvi, S. Type IV cracking behaviour of modified 9Cr-1Mo steel weld joints. *Mater. High Temp.* **2016**, *33*, 137–153. [CrossRef]
3. Falat, L.; Svoda, M.; Výrostková, A.; Petryshynets, I.; Sopko, M. Microstructure and creep characteristics of dissimilar T91/TP316H martensitic/austenitic welded joint with Ni-based weld metal. *Mater. Charact.* **2012**, *72*, 15–23. [CrossRef]
4. Tabuchi, M.; Hongo, H.; Abe, F. Creep Strength of Dissimilar Welded Joints Using High B-9Cr Steel for Advanced USC Boiler. *Met. Meter. Trans. A* **2014**, *45*, 5068–5075. [CrossRef]
5. Parker, J.D.; Stratford, G.C. Review of factors affecting condition assessment of nickel based transition joints. *Sci. Technol. Weld. Join.* **1999**, *4*, 29–39. [CrossRef]
6. Cao, J.; Gong, Y.; Yang, Z. Microstructural analysis on creep properties of dissimilar materials joints between T92 martensitic and HR3C austenitic steels. *Mater. Sci. Eng. A* **2011**, *528*, 6103–6111. [CrossRef]
7. Laha, K.; Chandravathi, K.S.; Rao, K.B.S.; Mannan, S.L.; Sastry, D.H. An Assessment of Creep Deformation and Fracture Behavior of 2.25Cr-1Mo Similar and Dissimilar Weld Joints. *Met. Meter. Trans. A* **2001**, *32*, 115–124. [CrossRef]
8. Zhang, Y.; Li, K.; Cai, Z.; Pan, J. Creep rupture properties of dissimilar metal weld between Inconel 617B and modified 9%Cr martensitic steel. *Mater. Sci. Eng. A* **2019**, *764*, 138185. [CrossRef]
9. Abson, D.J.; Rothwell, J.S. Review of type IV cracking of weldments in 9–12%Cr creep strength enhanced ferritic steels. *Int. Mater. Rev.* **2013**, *58*, 437–473. [CrossRef]
10. Kimmins, S.T.; Smith, D.J. On the relaxation of interface stresses during creep of ferritic steel weldments. *J. Strain Anal.* **1998**, *33*, 195–206. [CrossRef]
11. Kim, N.; Kang, Y.; Bang, J.; Song, S.; Seo, S.-M.; Kang, C.-Y.; Kang, N. Effect of Postweld Heat Treatments on Type IV Creep Failure in the Intercritical Heat-Affected Zone of 10% Cr Martensitic Steel Welded with Haynes 282 Filler. *Metals* **2021**, *11*, 726. [CrossRef]
12. Yamazaki, M.; Watanabe, T.; Hongo, H.; Tabuchi, M. Creep Rupture Properties of Welded Joint of Heat Resistant Steels. *J. Power Energy Syst.* **2008**, *2*, 1140–1149. [CrossRef]
13. Dupont, J.N. Microstructural evolution and high temperature failure of ferritic to austenitic dissimilar welds. *Int. Mater. Rev.* **2012**, *57*, 208–234. [CrossRef]
14. Parameswaran, P.; Laha, K. Role of Microstructure on Creep Rupture Behaviour of Similar and Dissimilar Joints of Modified 9Cr-1Mo Steel. *Procedia Eng.* **2013**, *55*, 438–442. [CrossRef]
15. Dupont, J.N.; Mizia, R.E. *Review of Dissimilar Metal Welding for the NGNP Helical-Coil Steam Generator*; Idaho National Laboratory: Idaho Falls, ID, USA, 2010.
16. Matsunaga, T.; Hongo, H.; Tabuchi, M. Interfacial failure in dissimilar weld joint of high boron 9% chromium steel and nickel-based alloy under high-temperature creep condition. *Mater. Sci. Eng. A* **2017**, *695*, 302–308. [CrossRef]
17. Klueh, R.L.; King, J.F. Austenitic Stainless Steel-Ferritic Steel Weld Joint Failures. *Weld. Res. Suppl.* **1982**, *61*, 302–311.
18. Shin, K.Y.; Lee, J.W.; Han, J.M.; Lee, K.W.; Kong, B.O.; Hong, H.U. Transition of creep damage region in dissimilar welds between Inconel 740H Ni-based superalloy and P92 ferritic/martensitic steel. *Mater. Charact.* **2018**, *139*, 144–152. [CrossRef]
19. Laha, K.; Chandravathi, K.S.; Parameswaran, P.; Goyal, S.; Mathew, M.D. A Comparison of Creep Rupture Strength of Ferritic/Austenitic Dissimilar Weld Joints of Different Grades of Cr-Mo Ferritic Steels. *Met. Meter. Trans. A* **2012**, *43*, 1174–1186. [CrossRef]
20. Kim, M.; Kang, Y.; Kim, N.; Lee, S.; Song, S.; Kang, N. PWHT Cracking Susceptibility in the HAZ of Martensitic 10Cr Steel for A-USC Power Plant. *Korean J. Met. Mater.* **2019**, *57*, 430–437. [CrossRef]
21. Dimmler, G.; Weinert, P.; Kozeschnik, E.; Cerjak, H. Quantification of the Laves phase in advanced 9–12% Cr steels using a standard SEM. *Mater. Charact.* **2003**, *51*, 341–352. [CrossRef]
22. Kumar, S.; Pandey, C.; Goyal, A. A microstructural and mechanical behavior study of heterogeneous P91 welded joint. *Int. J. Press. Vessel. Pip.* **2020**, *185*, 104128. [CrossRef]
23. Khajuria, A.; Kumar, R.; Bedi, R. Characterizing Creep Behaviour of Modified 9Cr1Mo Steel by using Small Punch Impression Technique for Thermal Powerplants. *J. Mech. Mech. Eng.* **2018**, *4*, 47–61.
24. Orzolek, S.; Dupont, J.; Siefert, J. Microstructural Evolution of Dissimilar Metal Welds Involving Grade 91. *Met. Meter. Trans. A* **2020**, *51*, 2222–2238. [CrossRef]
25. Switner, N.; Yu, Z. Austenitic Stainless Steel Cladding Interface Microstructures Evaluated for Petrochemical Applications. *Weld. J.* **2019**, *98*, 50–61.
26. Parker, J.D.; Stratford, G.C. Characterisation of microstructures in nickel based transition joints. *J. Mater. Sci.* **2000**, *35*, 4099–4107. [CrossRef]
27. Dai, T.; Lippold, J.C. The Effect of Postweld Heat Treatment on Hydrogen-Assisted Cracking of F22/625 Overlays. *Weld. J.* **2018**, *97*, 75–90.

28. Fedoseeva, A.; Dudova, N.; Kaibyshev, R. Creep strength breakdown and microstructure evolution in a 3%Co modified P92 steel. *Mater. Sci. Eng. A* **2016**, *654*, 1–12. [CrossRef]
29. Morita, S.; Saito, H.; Ogawa, T.; Furuhara, T.; Maki, T. Effect of Austenite Grain Size on the Morphology and Crystallography of Lath Martensite in Low Carbon Steels. *ISIJ Int.* **2005**, *45*, 91–94. [CrossRef]
30. Takaki, S.; Fukunaga, K.; Syarif, J.; Tsuchiyama, T. Effect of Grain Refinement on Thermal Stability of Metastable Austenitic Steel. *Mater. Trans.* **2004**, *45*, 2245–2251. [CrossRef]
31. Wang, Y.; Kannan, R.; Li, L. Insight into Type IV cracking in Grade 91 steel weldments. *Mater. Des.* **2020**, *190*, 108570. [CrossRef]
32. Celada-Casero, C.; Sietsma, J.; Santofimia, M.J. The role of the austenite grain size in the martensitic transformation in low carbon steels. *Mater. Des.* **2019**, *167*, 107625. [CrossRef]
33. Maruyama, K.; Sawada, K.; Koike, J. Strengthening Mechanisms of Creep Resistant Tempered Martensitic Steel. *ISIJ Int.* **2001**, *41*, 641–653. [CrossRef]
34. Klueh, R.L. Dissimilar metal weld failures in boiler tubing. *Power Eng.* **1984**, *88*, 52–56.
35. Gallo, P.; Sroka, M.; Razavi, S.M.J.; Peron, M.; Torgersen, J.; Berto, F. Creep behavior of V-notched components. *Frat. Ed. Integrità Strutt.* **2017**, *41*, 456–463. [CrossRef]
36. Gallo, P.; Berto, F.; Glinka, G. Generalized approach to estimation of strains and stresses at blunt V-notches under non-localized creep. *Fatigue Fract. Eng. Mater. Struct.* **2016**, *39*, 292–306. [CrossRef]